1   Revision 2

2   The origin of needle-like rutile inclusions in natural gem corundum: a combined

3   EPMA, LA-ICP-MS, and nanoSIMS investigation

4   Aaron C. Palke*[1,2,3] and Christopher M. Breeding[1]

5   1.   Gemological Institute of America, Carlsbad, CA 92011, USA

6   2.   Queensland Museum, Brisbane, QLD 4101, Australia

7   3.   University of Queensland, Brisbane, QLD 4072, Australia

8   *aaron.palke@qm.qld.gov.au

9   **Abstract**

10   Trace element chemistry and microscopic observations of included gem corundum (α-Al$_2$O$_3$)

11   suggests a new model of syngenetic growth of oriented rutile inclusions rather than the usual

12   interpretation of their growth through exsolution. Laser Ablation Inductively Coupled Plasma Mass

13   Spectrometry (LA-ICP-MS) is now a robust method for measuring trace elements in gem quality

14   corundum (ruby and sapphire). Nonetheless, the corundum structure is relatively unforgiving for

15   substitutional components and typically only a small handful of minor to trace elements are measured

16   by LA-ICP-MS (Mg, Ti, V, Cr, Fe, Ga). Less commonly, trace elements such as Be, Zr, Nb, Sn, La, Ce, Ta,

17   and W are found in natural corundum. Their concentrations are typically correlated with high contents

18   of Ti and silky or cloudy zones in the corundum that contain a high concentration of needle-like rutile or

19   other oxide inclusions. Three metamorphic-type sapphires from Sri Lanka, Madagascar, and Tanzania

20   were studied here using LA-ICP-MS, Electron Probe MicroAnalysis (EPMA), and nanoSIMS to document

21   correlations between the various trace elements and their distribution between the corundum and

1

22   included, oriented rutile TiO_2 needles. NanoSIMS and EPMA measurements show concentration of Be,

23   Mg, Fe, V, Zr, Nb, Ce, Ta, and W in the rutile needles. The relative atomic concentrations of Mg and Ti

24   from LA-ICP-MS measurements suggest the corundum-rutile intergrowth grew as a mechanical mixture

25   of the two phases as opposed to rutile formation through exsolution from the corundum host. This

26   scenario is also suggested for the three magmatic-type sapphires studied here based on the presence of

27   glassy melt inclusions in close association with included, oriented oxide needles. The preservation of a

28   glassy melt inclusion requires fast cooling whereas exsolution of the oxide inclusions would require slow

29   cooling and annealing at a temperature lower than sapphire formation. The studied sapphires suggest

30   the likely origin of the oriented, needle-like rutile inclusions to be syngenetic epitaxial coprecipitation of

31   both rutile and corundum. The interpretation of such oriented oxide inclusions has important

32   implications for understanding the geological formation conditions based on trace element data or using

33   such data to separate sapphires and rubies based on their geographic origin.

34   **Keywords**: corundum, sapphire, exsolution, immiscibility, gemology, trace element chemistry, melt

35   inclusions, nanoSIMS, LA-ICP-MS, EPMA, rutile inclusions

36   **Introduction**

37   Oriented, needle-shaped oxides are among the most common inclusions in gem-quality

38   corundum, Al_2O_3 (ruby and sapphire). Frequently encountered oriented oxide inclusions include rutile

39   (TiO_2), hematite (Fe_2O_3), and ilmenite ($FeTiO_3$) and more rarely pseudobrookite, an Fe,Ti oxide (Hughes

40   1997; Izokh et al. 2010). Oriented rutile needles are generally aligned in the basal plane (perpendicular

41   to the c-axis) and parallel to the crystallographic directions of the second order hexagonal prism and

42   hematite and ilmenite reportedly form in the basal plane of the first order prism with oriented needles

43   in both cases intersecting themselves at an angle of 60°/120° (Hughes 1997). Except for star rubies and

44   sapphires, such inclusions, in general, are considered to detract from the gem's value. However, the

2

45   advent of heat treatment of sapphires to extreme temperatures (often around 1500 °C or more) starting

46   in the 1960's relied on the dissolution of TiO_2 needles to enhance the blue coloration of otherwise

47   worthless, milky "geuda" corundum (Emmett et al. 2003). The underlying mechanism in this case is the

48   dissolution of rutile inclusions and the incorporation of Ti^{4+} into the corundum lattice to pair with Fe^{2+}

49   causing blue color through absorption of visible light by an Fe^{2+}-Ti^{4+} intervalence-charge transfer (e.g.

50   Emmett and Douthit 1993).

51   Phenomenal star sapphires and rubies rely on the presence of such oriented needle-like

52   inclusions to produce asterism. In fact, synthetic star sapphires and rubies have been produced for many

53   decades by dissolving Ti into synthetic corundum at very high temperatures (~1800 °C, Schmetzer et al.

54   2015) and subsequently annealing at a lower temperature to exsolve TiO_2 needles. At first glance, the

55   ability to both dissolve and precipitate rutile needles at high temperature seems to support the

56   hypothesis that such oriented oxide needles originate in natural gem corundum through exsolution by

57   slowly cooling from the temperature of formation. Indeed, this origin is generally accepted for natural

58   gem-quality corundum in much of the gemological and geological literature (e.g. Moon and Phillips

59   1984; De Maesschalck and Oen 1989; Guo et al. 1996; Upton et al. 1999; Sutherland et al. 2002, 2009).

60   However, the exsolution hypothesis for oriented oxide inclusions in natural corundum has not been

61   rigorously tested. It should be pointed out that the temperatures of natural corundum formation (500-

62   800 °C for metamorphic corundum, e.g. Giuliani et al. 2014) are generally much lower than those

63   involved in heat-treatment of natural corundum (>1500 °C, Emmet and Douthit 1993), and so the ability

64   to dissolve TiO_2 into Al_2O_3 at such high temperatures is not proof of exsolution in natural untreated

65   stones. Similarly, the annealing and exsolution in synthetic star sapphires and rubies occurs from 1100-

66   1500 °C (Schmetzer et al. 2015). Therefore, the ability to exsolve oriented rutile needles in such material

67   does not necessarily indicate that the same process is responsible for oriented oxide inclusions in

68   natural sapphires which formed at much lower temperatures. It should be noted that, while much of the

3

69   literature accepts an exsolution mechanism, McGee (2005) interpreted the presence of oriented rutile

70   inclusions in sapphires from Tasmania, Australia to be the product of coprecipitation of rutile with

71   corundum due to the pattern of rutile orientation in relation to the corundum growth zoning.

72   **Background**

73   A possible mechanism allowing for rutile dissolution in corundum is fairly straightforward.

74   When Ti^{4+} substitutes for Al^{3+} in corundum, divalent cations such as Mg^{2+} or Fe^{2+} act as charge

75   compensators:

76    $2Al^{3+} = Fe^{2+} + Ti^{4+}$ (1).
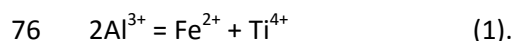
77   Natural corundum always contains trace to minor amounts of Fe, typically in excess of the atomic

78   concentrations of Ti. This excess Fe can enter the corundum lattice through an isovalent substitution of

79   Fe^{3+} for Al^{3+}. Therefore, if rutile-included corundum is heated at high temperature under reducing

80   conditions, Ti^{4+} from rutile inclusions can dissolve into corundum through reduction of Fe^{3+} to Fe^{2+} to

81   provide charge compensation when Ti^{4+} substitutes for Al^{3+}:

82    $Ti^{4+}_{rutile} + Fe^{3+}_{corundum} + e^{-} = Ti^{4+}_{corundum} + Fe^{2+}_{corundum+}$ (2),
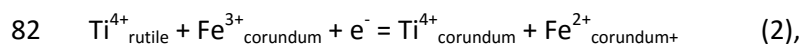
83   with " e^{-} " on the left-hand side potentially representing an electron from hydrogen which could then

84   enter the corundum lattice as a hydroxyl group (Emmett and Douthit 1993; Beran and Rossman 2006).

85   Exsolution of rutile from corundum can be envisaged as being the reversal of this reaction through

86   slowly cooling or annealing at a temperature lower than that at which the corundum formed. Several

87   TEM investigations of natural (Moon and Phillips 1984) and synthetic (Phillips et al. 1980a, b, c) star

88   sapphires described the crystallographic orientations of their oxide inclusions. Moon and Phillips (1984)

89   also showed that in natural, Fe-rich black star sapphires the oriented needle-like inclusions are

90   composed of a variety of Fe/Ti oxides and not just rutile. More recent TEM experiments by Shen and

4

91 Wirth (2012) showed that Ti-rich clouds in some natural sapphires are composed of minute (20-40 nm

92 long and 5-10 nm wide) TiO_2 nano-inclusions taking the α-PbO_2 structure.

93   Many research efforts have been devoted to elucidating the formation of oriented oxide

94 needles in other refractory minerals such as garnets (Hwang et al. 2007; Ague and Eckert 2012; Hwang

95 et al. 2015) where such a simple exsolution/dissolution reaction does not present itself. TiO_2 can be a

96 minor or major component of many garnets. In such a multicomponent mineral with more than three

97 cationic coordination sites, there is no easy path to the removal of a component from one cation site

98 without altering the fundamental stoichiometry of the mineral or without external input of some other

99 component to compensate removal of Ti^{4+} cations from the garnet lattice. The complications of applying

100 the exsolution hypothesis to the phenomenon of oriented oxide needles in garnets has led many

101 researchers to suggest their formation through processes such as alteration of inherited precursor

102 minerals or later formation of rutile through interaction with fluids or melts entering along oriented

103 cracks or cleavages forming along planes of weakness in the garnet structure (Hwang et al. 2007). On

104 the other hand, Ague and Eckert (2012) demonstrated that oriented rutile in some garnets are the

105 product of exsolution based on the observation of diffusion haloes of Ti around oriented inclusions,

106 even if the mechanism of exsolution is unclear. However, Hwang et al. (2015) provided evidence that

107 oriented rutile inclusions in star garnets are the product of simultaneous coprecipitation of rutile and

108 garnet.

109   In this contribution we present two independent lines of evidence suggesting that, in many

110 cases, the hypothesis of exsolution of oriented oxide inclusions in gem corundum is unlikely if not

111 untenable. Firstly, we present chemical evidence from Electron Probe MicroAnalysis (EPMA), Laser

112 Ablation Inductively Coupled Plasma Mass Spectrometry (LA-ICP-MS), and nano-Secondary Ion Mass

113 Spectrometry (nanoSIMS) detailing the distribution of "unusual" trace elements (Be, rare-earth

5

114   elements [REE] and high-field strength elements [HFSE] such as Zr, Nb, Ta, W) in gem corundum from

115   several deposits. Such trace elements are occasionally detected in gem corundum using SIMS and LA-

116   ICP-MS (e.g. Upton et al. 1999; McGee 2005; Lu and Shen 2011; Shen and Wirth 2012). These trace

117   elements are hereafter described using the term "unusual trace elements" given that they have ionic

118   radii and/or cation charges significantly different than $^{VI}Al^{3+}$ and so they are not expected to substitute

119   readily into the corundum lattice and so their measurement is "unusual". Furthermore, their presence is

120   generally correlated with elevated concentrations of Ti and often with regions in the corundum that are

121   "cloudy" due to a high density of particulate inclusions (Lu and Shen 2011; Shen and Wirth 2012). Our

122   EPMA and nanoSIMS microanalysis confirms the presence of these "unusual" trace elements in rutile

123   inclusions and not in the corundum lattice. In fact, most of these trace elements are known to be highly

124   compatible in rutile (e.g. Zack et al. 2002) and so their presence here suggests that they may have been

125   originally incorporated in oriented rutile inclusions which coprecipitated with the corundum.

126   The second line of evidence presented here is the microscopic observation of oriented rutile

127   inclusions along with glassy melt inclusions in sapphires from the volcanic-associated deposits of Rock

128   Creek and Missouri River, Montana, USA and the Anakie gem fields of Queensland, Australia. Exsolution

129   of rutile or other oxide inclusions occurs only when the corundum host is held at a temperature lower

130   than that of the initial formation for an extended period of time to allow for the oriented inclusions to

131   nucleate and grow through solid state diffusion. On the other hand, preservation of glassy melt

132   inclusions necessitates rapid cooling of the corundum containing the melt inclusions to prevent

133   nucleation and crystal growth from the melt. Taken together, the observations presented here provide

134   strong evidence against the hypothesis of exsolution in at least some gem corundum.

135   **Methods**

136   **Materials**

6

137   Sapphires from Tunduru, Tanzania; Elahera, Sri Lanka; Andranondambo, Madagascar, and

138   Anakie, Australia were collected by field gemologist Vincent Pardieu from the Gemological Institute of

139   America (GIA). Sample names used here (see below) correlate to GIA reference collection numbers as

140   follows: TUN – 669320802, ELA – 669233502, AND – 669116302, ANA – AC747. Samples MIS and ROC

141   are from one author's personal collection (AP).

142   **Electron Probe MicroAnalysis (EPMA)**

143   EPMA was performed at Caltech on a JEOL JXA-8200 at Caltech in Pasadena, CA with an

144   accelerating voltage of 15 kV and a nominal 0 μm focused beam of 40 nA. Off- and on-peak X-rays were

145   counted for 20 s for Ti Kα, Fe Kα, Cr Kα, 25 s for Nb Lα, Zr Lα, Ce Lα, 30 s for W Lα, Ta Lα, 40 s for V Kα,

146   and 80 s for Mg Kα and Al Kα. Standards employed were tantalum metal (Ta), tungsten metal (W),

147    $CePO_4$ (Ce), synthetic fayalite (Fe), Pacoima zircon (Zr), MgO (Mg), Al_2O_3 (Al), TiO_2 (Ti), V_2O_5 (V), Cr_2O_3

148   (Cr), and NbO (Nb). Analytical uncertainty is estimated at <1% error for major elements and up to 10%

149   for trace elements.

150   **Laser Ablation Inductively Coupled Plasma Mass Spectrometry (LA-ICP-MS)**

151   LA-ICP-MS sapphire analyses were performed at the Gemological Institute of America in

152   Carlsbad, CA on a Thermo Scientific iCap-Q ICP-MS with plasma rf power of 1400 W coupled with a New

153   Wave Research UP-213 laser ablation unit with a frequency-quintupled Nd:YAG laser (213 nm

154   wavelength with 4 ns pulse width). A laser spot-size of 55 μm was used with a fluence of 10±1 J/cm^2 and

155   15 Hz repetition rate. NIST 610 and 612 glasses were used for standardization using ^{27}Al as an internal

156   standard. Isotopes measured are ^9Be, ^{24}Mg, ^{47}Ti, ^{51}V, ^{52}Cr, ^{57}Fe, ^{71}Ga, ^{91}Zr, ^{93}Nb, ^{140}Ce, ^{181}Ta, and ^{182}W.

157   Standard deviations for the measurements are given in **Tables 1A-C** and in the appendix in **Tables S1A-C**.

158   Detection limits were calculated from the standard deviation and the total number of data points

159   collected on both the gas blank and the sample for the first unknown analyzed and this detection limit

7

160   was taken to represent the detection limit for subsequent analyses. The quantitation limit was taken as

161   3.33×detection limit.

162   **NanoSIMS**

163   To investigate trace element distribution and quantify Be concentration, ion imaging and depth

164   profiling were performed with the Cameca NanoSIMS 50L at Caltech in Pasadena, CA. Samples were

165   coated with an Au layer of 20 nm. A -8 keV and 250-500 pA O- primary ion beam was used to raster in

166   squares of 5 μm × 5 μm across the sample surface. Positive 8 keV secondary ions of ^{9}Be, ^{50}Ti, ^{56}Fe, ^{181}Ta,

167   and ^{186}W were simultaneously collected only from the center 2.5 × 2.5 μm areas with electron

168   multipliers. A ^{9}Be-implanted TiO_2 wafer was produced as a standard to quantify Be concentrations in

169   TiO_2 inclusions. Double-side polished TiO_2 wafers of 1 cm × 1 cm × 0.1 cm were purchased from MTI

170   Corporation. ^{9}Be was implanted by Innovion Corporation with a fluence of 10^{16} atoms/cm^2 at an implant

171   energy of 50 keV. Implanted wafers were measured using the same NanoSIMS analytical protocols as

172   above. The peak depth of the implants was calculated using the SRIM software (Ziegler et al. 2010).

173   **Raman Spectroscopy**

174   Raman spectra were collected with a Renishaw inVia Raman microscope system. The Raman

175   spectra of the inclusions were excited by a Stellar-REN Modu Ar-ion laser at 514 nm and collected at a

176   nominal resolution of 3 cm–1 in the 2000–200 cm–1 range. Each spectrum of the inclusions was

177   accumulated three times. for 10 s each at 20× or 50× magnification. Confocal optics allowed inclusions

178   beneath the surface to be analyzed without having to polish through the inclusion and without

179   significant interference from the host corundum.

180   **Results**

181   **Microscopic Observations of Melt Inclusions and Oriented Oxide Inclusions**

       8

182   Microscopic observations of melt inclusions coexisting with oriented rutile inclusions in gem

183   corundum were made on three samples: MIS, a sapphire from the Missouri River deposit in Montana,

184   USA; ROC, a sapphire from the Rock Creek district of Montana, USA; and ANA, a sapphire from the

185   Anakie gem fields of Queensland, Australia. Sapphires in all three deposits are generally recognized to

186   have been transported to the surface by geologically recent volcanic activity – Cenozoic in the case of

187   both the Montana deposits (Berg and Dahy 2002; Berger and Berg 2006) and the Anakie gem fields

188   (Robertson and Sutherland 1992). The sapphires are, nonetheless, considered to be xenocrysts in the

189   host volcanic rocks. Photomicrographs documenting the relationships described below are shown in

190   **Figures 1a-d**. The oriented rutile inclusions in all three cases occur in three directions and needles

191   intersect each other at a 60° angle (identity of rutile needles confirmed by Raman spectroscopy). Glassy

192   melt inclusions are observed in all three samples in intimate association with oriented rutile needles. In

193   sample MIS the density of oriented rutile inclusions is low, but the melt inclusion appears to be

194   completely glassy and homogeneous except for a bubble in one corner of the inclusion. The other

195   sapphires have much higher density of rutile inclusions occurring in discrete zones of the sapphires.

196   Except for a few thin planes of oriented needles in ROC, these sapphires show abrupt transitions to

197   inclusion-free sapphire (**Figure 1a**). Also, except for unidentified, opaque black inclusions in some of the

198   melt inclusions for ROC and ANA, the inclusions are completely glassy without any signs of

199   devitrification. In all cases microscopic observations suggest that the glassy melt inclusions are primary.

200   For instance, the melt inclusions all occur far from the edges of the sapphire grains and they occur

201   sufficiently far from fractures or other inclusions (except oriented oxide inclusions). Additionally, in

202   sample ANA the melt inclusions all occur right on the sharp boundary between the densely included

203   area and the particle-free area suggesting they were all included at a specific time during the growth of

204   the corundum.

205   **Trace Element Chemistry**

9

206   **Sample descriptions.** Three samples were analyzed here: AND, ELA, and TUN. Sample AND is a

207   broken piece of a hexagonal, barrel-shaped crystal from Andranondambo, Madagascar. Sapphires from

208   this deposit are associated with skarn formations (Rakotondrazafy et al. 2008). Sample AND has a cloudy

209   core with a dense package of oriented oxide inclusions (**Figure 2a**). A sharp boundary separates this core

210   from a blue inclusion-free rim (**Figure 2b**). Additionally, there are several thin bands of particle-rich

211   areas separated by particle-free sections. Sample ELA is a hexagonal polished plate with patches of

212   cloudy included areas near the core and a transparent inclusion-free rim (**Figures 2c-d**). The sample was

213   collected from the Elahera gem field of Sri Lanka. This is an alluvial deposit which is also generally

214   associated with skarn formations (Silva and Siriwardena 1988) and high-grade metamorphic formations.

215   Sample TUN is an oblate, rounded polished plate with a central, dark brown, included core surrounded

216   by transparent inclusion-free sapphire interrupted occasionally by linear patches of included areas

217   (**Figures 2e-f**). The Tunduru gem field is also an alluvial deposit, but is also associated with high-grade

218   metamorphic rocks belonging to the Mozambique Metamorphic Belt (Chitty 2009). Raman spectra

219   collected on the oriented oxide inclusions observed in these three samples allowed them to be

220   identified as rutile.

221   **LA-ICP-MS.** Laser ablation analyses were profiled across the samples in sub-linear arrays of sub-

222   regularly-spaced spots. In all cases two passes were made in certain areas. The ablation spots were

223   documented with the photomicrographs in **Figures 2a-f** and the LA-ICP-MS results for select trace

224   elements are displayed in **Figure 3** and the full analyses in **Tables 1a-c** for atomic ppm and in **Tables S1a-**

225   **c** for ppm by weight.

226   Comparing the photomicrographs of **Figures 2a-f** and the LA-ICP-MS trace element profiles of

227   **Figure 3** shows an obvious correlation between the cloudy areas containing oriented oxide inclusions

228   and primarily Ti but also Mg and Fe and the trace elements such as Be, Ce, Ta, Nb, Zr, and W. In most

10

229   cases, Ta and W dominate with subordinate amounts of Nb, Zr, and Be. In general, Ti contents are within

230   the range of 10-135 atomic parts per million (ppma) in the inclusion-free areas but up to 741 ppma in

231   the cloudy areas. Ta and W contents can reach up to 40 ppma and 27 ppma, respectively, in the cloudy,

232   included areas. Be, REE's, Nb, and Zr are typically less than 10 ppma when present, except for Be which

233   ranged up to 27 ppma in one spot in ELA. In general, all the elements analyzed here except Cr (when

234   detected), show a distinct, positive correlation with Ti concentrations.

235   **Figure 4** shows plots of ppma Mg vs Ti for AND, TUN, and ELA. At low concentrations ppma Ti

236   and Mg fall closely along a 1:1 line. Then above about 70 ppma Ti for AND and about 160 ppma Ti for

237   TUN and ELA, the data fall to the right of the 1:1 line with Ti concentrations continuing to increase with

238   little to no concomitant increase in Mg concentrations. This suggests that when low concentrations of Ti

239   are measured the Ti^{4+} is incorporated into the corundum lattice through a charge-coupled substitution

240   with Mg^{2+}:

241

242    $2Al^{3+} = Mg^{2+} + Ti^{4+}$ (3).
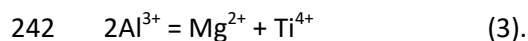
243

244   The measurement by LA-ICP-MS of Ti concentrations above the threshold values described above seems

245   to indicate incorporation of Ti in the system in some other way. Note that the threshold value is much

246   lower for AND than for TUN and ELA. This is likely due to a charge-coupled substitution of Ti^{4+} by Fe^{2+} as

247   well as Mg^{2+}. This is evidenced by the blue color seen in sample AND which is caused by optical

248   absorption related to intervalence charge transfer between Fe^{2+} and Ti^{4+}. Samples ELA and TUN have no

249   discernible blue coloration and so a charge-coupled substitution of Fe^{2+} and Ti^{4+} is probably not

250   significant.

11

251   **EPMA results.** Backscattered electron imaging revealed the presence of oriented rutile needles

252   only in samples TUN and ELA. Unfortunately, no oriented rutile needles could be detected in sample

253   AND. This is likely due to the overall lower density of rutile needles as evidenced by the relatively lower

254   Ti concentration in this sample, and also due to the overall smaller size of such inclusions as roughly

255   measured from our photomicrographs (~0.5 μm in AND and ~2 μm in TUN and ELA). Even in TUN and

256   ELA, however, the rutile inclusions were not large enough for clean analyses to be obtained. Inevitably,

257   even using a focused (nominal) 0 μm beam, the EPMA measurements indicated from 17-30 wt% Al_2O_3

258   for TUN and 63-69 wt% Al_2O_3 for ELA. Given the low levels of solubility of TiO_2 into Al_2O_3 and of Al_2O_3

259   into TiO_2 (Roy and Coble 1968; Pownceby et al. 2003), it should be possible to deduce the chemistry of

260   the rutile inclusions by subtracting the Al_2O_3 component. Given the low concentrations of trace

261   elements in corundum from LA-ICP-MS measurements (>99.8 wt% Al_2O_3 for TUN and ELA), it can be

262   assumed that the other elements measured by EPMA (i.e. MgO, FeO, V_2O_3, Nb_2O_5, Ta_2O_5, WO_3) are

263   contained within the rutile inclusions and so simple subtraction of Al_2O_3 from the EPMA measurements

264   and renormalization to 100 wt% should produce an accurate representation of the chemistry of the

265   rutile inclusions. It should be noted that the raw data totals to 99-101 wt%. EPMA measurements on

266   oriented rutile inclusions in samples TUN and ELA obtained in this way are reported in Table 2. Assuming

267   all iron is incorporated as Fe^{2+}, analyses can be converted to stoichiometric rutile formulas with full

268   occupation of one octahedral cation site per two oxygens.

269   Rutile in TUN contains a large amount of Ta^{5+} with 20.4-22.4 wt% Ta_2O_5 or 0.084-0.094 atoms

270   Ta^{5+} per formula unit (2 O atoms) with lesser concentrations of Nb_2O_5 from 1.3-1.5 wt% or 0.009-0.011

271   atoms Nb^{5+} per formula unit. The high Ta content in rutile inclusions in TUN is notable and is in the

272   higher realm of Ta substitution in natural rutile which has been reported at up to 34 wt% Ta_2O_5 in rare

273   occurrences (Hoe et al. 2007). The total atoms of Nb^{5+} + Ta^{5+} is close to twice the number of atoms of

274   Mg^{2+} + Fe^{2+} suggesting the following charge-coupled substitution mechanism:

12

275

276     $3Ti^{4+} = 2(Nb^{5+},Ta^{5+}) + (Mg^{2+},Fe^{2+})$ (4).
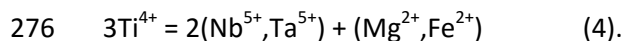
277

278   The rutile in TUN also contains a small amount of V_2O_3 (0.11-0.39 wt%) and in one inclusion quantifiable

279   concentrations of ZrO_2 and CeO_2 (0.45 and 0.32 wt%, respectively). Note that while Ta_2O_5 was readily

280   measured by EPMA in the rutile inclusions, WO_3 was consistently below the detection limit for this

281   sample. This is at odds with the significant concentrations of W measured by LA-ICP-MS analysis.

282   Therefore, it is likely that W is hosted in some other nano- or micro-inclusion contained in the corundum

283   crystals and is not directly hosted in rutile inclusions.

284   In sample ELA, the rutile inclusions are nearly pure TiO_2 with 0.4-0.8 wt% FeO, 0.9-3.8 wt%

285   Ta_2O_5, 0.0-0.6 wt% Nb_2O_5, 0.3-0.4 wt% ZrO_2, and 0.3-0.4 wt% CeO_2. The much lower concentrations of

286   these trace elements relative to sample TUN is in general agreement with the LA-ICP-MS data which

287   shows much lower amounts of these species but similar Ti concentrations. The atomic concentrations of

288   Mg, Fe, Nb, and Ta do not generally seem to follow equation 4 mentioned above. This is probably, in

289   part, due to the lower concentrations of these species and, hence, the greater analytical uncertainty

290   associated with their measurement. However, there is generally more Fe present than needed by

291   equation 4 which may mean that some of the iron is present as Fe^{3+} which requires less Nb^{5+} or Ta^{5+} for

292   charge balance. Finally, there is W^{6+} present in at least some of these rutile inclusions which can also aid

293   in the charge-balancing of Fe and Mg in rutile.

294   **nanoSIMS results.** Representative nanoSIMS raster maps for samples TUN and AND are shown

295   in **Figures 5a-b**. In both cases rutile inclusions could be imaged as isolated enrichments in ^{50}Ti. For

296   sample TUN the rutile inclusions also show elevated levels of ^{56}Fe and ^{181}Ta in agreement with EPMA

13

297 measurements described above. ^{56}Fe was also found enriched in the rutile inclusions in AND but without

298 measurable ^{181}Ta. This finding is in line with the low concentrations of Ta determined by LA-ICP-MS

299 analysis. ^{9}Be was also measured in the rutile inclusions in AND and TUN with much higher

300 concentrations in sample AND. Despite the relatively high concentrations of tungsten measured in

301 sample AND and TUN by LA-ICP-MS (up to 12 ppma for AND and 27 ppma for TUN) ^{186}W could not be

302 detected in any of the samples. While some tungsten was detected in rutile inclusions in sample ELA, it

303 was present at a relatively low concentration, so any tungsten in the rutile inclusions described here

304 may simply be at levels below the detection limit of nanoSIMS. Note also that ^{186}W should be harder to

305 detect than ^{181}Ta due to the lower isotopic abundance of ^{186}W.Alternatively, as suggested above for

306 sample TUN, it may be that W is not hosted in rutile inclusions but is contained in some other type of

307 nano- or micro-inclusion in these samples.

308   Sample ELA was analyzed and rutile inclusions were imaged in ^{50}Ti maps; however, except for

309 enrichment in ^{56}Fe in the rutile inclusions, no other trace elements could be detected. Again, this is

310 reasonable given the relatively low concentrations of Ta and W in sample ELA. While Be was actually at

311 higher concentrations in ELA than the other samples studied here, Be was unevenly distributed so it may

312 simply be that Be is contained in some rutile inclusions in this sample that were not analyzed by our

313 nanoSIMS measurements. Alternatively, the possibility exists that Be in this sample may be included in

314 some other type of inclusion altogether. In fact, looking at the data in **Table 1B** and **Figure 3**, it appears

315 that there is actually a much closer correlation between Be and Mg rather than Be and Ti. Furthermore,

316 in two spots in the cloudy regions of this sample, the atomic concentration of Mg actually exceeds that

317 of Ti. Given the low concentration of Mg found in rutile inclusions by EPMA here, it then seems likely

318 that there is some other type of nano- or micro-inclusion that contains Mg in these cloudy regions. This

319 possible included phase may also incorporate Be in this sample.

14

320   Ion implanted wafers were used to quantitatively measure the Be concentrations in rutile

321   inclusions in samples AND and TUN. $^9Be/^{50}Ti$ sensitivity was measured from profiles on the ion

322   implanted wafers. Then, the counts of $^9Be/^{50}Ti$ in the nanoSIMS maps were integrated for the rutile

323   inclusions as delineated by the ^{50}Ti distributions. For sample TUN Be was measured up to about 0.001-

324   0.002 atoms per TiO_2 formula unit while for AND Be was measured from about 0.008-0.016 atoms per

325   formula unit corresponding to about 110-230 ppmw Be in TUN and 700-2300 ppmw Be in AND. It should

326   be noted that these concentrations were calculated assuming the inclusions are nearly pure TiO_2

327   inclusions. However, the EPMA measurements for TUN have shown that around 10 atomic % Ti can be

328   substituted by other elements. LA-ICP-MS analyses for AND also show a significant amount of W which is

329   likely contained in the rutile inclusions as well. In fact, the LA-ICP-MS analyses show atomic ratios of

330   W/Ti at about 0.08-0.12 suggesting the rutile inclusions in this sample may also contain about 10 atom %

331   deficiency of Ti. In this case our atomic Be measurements would be overestimated by about the same

332   amount. More accurate nanoSIMS measurements would require the development of standards for

333   other expected elements in the rutile inclusions.

334   For sample AND the atomic ratios of Be/Ti from the LA-ICP-MS analyses (0.008) in the region of

335   the nanoSIMS analyses are in the same range as the Be/Ti ratio given by our nanoSIMS measurements

336   (0.008-0.016) suggesting that most if not all of the Ti and Be in the cloudy regions of these samples is

337   contained in the oriented rutile inclusions. For sample TUN, the nanoSIMS measurements were not

338   made in the region of the sample in which Be was detected by LA-ICP-MS and so comparisons cannot be

339   directly made between LA-ICP-MS and nanoSIMS analyses.

340   **Discussion**

341   The presence of glassy melt inclusions closely associated with oriented rutile inclusions in

342   samples ROC, MIS, and ANA seems to contradict an origin of the rutile by exsolution from corundum.

15

343   Many sapphires from the Anakie, Rock Creek, and Missouri River deposits have been examined by the

344   first author (AP) and several stones have been found with melt inclusions as well as silicate mineral

345   inclusions (phlogopite, feldspar, zircon, clinozoisite). Additionally, microscopic observations suggest the

346   melt inclusions are primary and not secondary inclusions. The liquid trapped in these inclusions, then,

347   most likely represents a melt lying on the liquidus in equilibrium with one or more silicate minerals.

348   Therefore, any further cooling after the melt is isolated in the corundum should result in precipitation of

349   one or more silicate minerals. The only way to preserve a glassy melt inclusion is to cool the corundum

350   containing the inclusion quickly, i.e. to quench to corundum.

351   On the other hand, exsolution of rutile or other oxide inclusions from corundum requires

352   formation of corundum at a relatively high temperature and then cooling and annealing at a lower

353   temperature at which the solubility of Ti is lower. The annealing temperature should also be

354   considerably lower in order to decrease Ti solubility enough so that the driving force of Ti oversaturation

355   can overcome the energetic barrier of rutile nucleation.

356   These two scenarios are hard to reconcile. Microscopic observation suggests that the melt

357   inclusions are primary inclusions (far from edges of the corundum crystals and no other nearby melt

358   inclusions) and so the melt inclusions were entrapped at the same time as corundum formation.

359   Therefore, if the corundum is cooled slowly and annealed at a lower temperature (but held at a high

360   enough temperature to allow diffusion of Ti), the glassy nature of the melt inclusions will almost

361   certainly not be preserved but will precipitate silicate minerals. One possible objection is that the

362   sapphires grew with primary melt inclusions, then cooled to exsolve rutile, and were subsequently

363   reheated by another magma which transported them to the surface. In this case one might expect a

364   recrystallized melt inclusion to be remelted if the sapphire were brought to or past its initial

365   temperature of formation. However, if the oxide inclusions formed through exsolution, one would

16

366   expect that they should redissolve when heated past their formation temperature. In this case these

367   particles should exhibit a blue halo of color due to the creation of Fe^{2+}-Ti^{4+} pairs as seen in heat-treated

368   sapphires where such particles have begun to dissolve into the corundum lattice (e.g. Gübelin and

369   Koivula 2008; Zwaan et al. 2015). Such blue haloes are not seen around any of the rutile inclusions in

370   these samples. Emmett and Douthit (1993) have shown that rutile dissolution and the creation of blue

371   haloes can occur in as little as 1 hour in heat treated samples. It seems, therefore, that if the rutile

372   needles were originally exsolved, some degree of redissolution should have taken place with a resultant

373   blue coloration showing accommodation of Ti^{4+} back into the corundum. The hypothesis of exsolution of

374   rutile inclusions in these specific corundum samples, then, seems to be untenable. We would suggest,

375   alternatively, that the oriented rutile inclusions in these samples may represent syngenetic epitaxial

376   coprecipitation of rutile and corundum.

377   While the observations above cannot be used as proof of coprecipitation of oriented oxide

378   inclusions in all natural corundum in general, they can be taken as evidence that the coprecipitation

379   hypothesis should be considered for oriented rutile inclusions in the other sapphires studied here (AND,

380   TUN, ELA). In fact, the Mg vs. Ti plots in **Figure 4** seem to corroborate this hypothesis. At low atomic

381   concentrations, Ti and Mg plot along a 1:1 line suggesting that Ti^{4+} is incorporated into corundum

382   through a charge-coupled substitution with Mg^{2+}. Note that there are, hypothetically, multiple charge-

383   coupled substitutions available for both Mg^{2+} and Ti^{4+} in corundum. Mg^{2+} could be charge compensated

384   by high field strength elements such as Ta^{5+} or W^{6+}. However, substitutions of this nature would push

385   the data points to the left of the 1:1 line in **Figure 4** and few data points lie significantly far into this

386   region. On the other hand, Ti^{4+} hypothetically can be charge compensated by Fe^{2+}. In fact, some charge

387   compensation of Ti^{4+} by Fe^{2+} is occurring in the particle-free rim of sample AND as evidenced by its blue

388   coloration. However, the fact that data points for the particle-free regions of these samples lie closely

389   along the 1:1 line in **Figure 4**, even though there is sufficient Fe in these regions to charge compensate

17

390   large amounts of Ti^{4+} (100-1000 ppma Fe in these samples) suggests that Ti^{4+} is dominantly incorporated

391   into corundum through coupled substitution with Mg^{2+} and that coupled substitution of Fe^{2+} and Ti^{4+} is

392   limited relative to substitution with Mg^{2+}. If the Ti contained in the rutile inclusions were originally

393   dissolved in the corundum lattice, this 1:1 correlation between ppma Ti and Mg should hold to higher

394   concentrations. However, the coprecipitation hypothesis is more consistent with the LA-ICP-MS data in

395   **Figure 4** in that LA-ICP-MS measurements on a coprecipitated mixture of rutile and corundum would fall

396   to the right of the 1:1 line as they represent analyses of corundum with a mechanical mixture of TiO_2

397   inclusions.

398   Furthermore, our documentation of the incorporation of high-field strength elements into the

399   oriented rutile inclusions also seems to corroborate an origin for the inclusions by coprecipitation and

400   not exsolution. In order for rutile to be exsolved with high concentrations of high-field strength

401   elements such as Zr^{4+}, Nb^{5+}, Ta^{5+}, W^{6+}, and Ce^{4+}, those elements must have been incorporated in the

402   corundum lattice initially along with Ti^{4+}. One initial assumption is that the high-field strength elements

403   analyzed by LA-ICP-MS should be too large and/or too highly-charged to be accepted in the corundum

404   lattice. **Table 3** provides the ionic radii of the cations which are potentially incorporated into corundum

405   or rutile from this study (Shannon 1976). This data shows that many of the cations which are generally

406   acknowledged to substitute for Al^{3+} in the corundum lattice (Mg^{2+}, Ti^{4+}, V^{3+}, Cr^{3+}, Fe^{2+}, Fe^{3+}, Ga^{3+}), actually

407   have ionic radii similar to the high-field strength elements observed here such as Zr^{4+}, Nb^{5+}, Ta^{5+}, and

408   W^{6+}. For instance, $^{VI}Ta^{5+}$ and $^{VI}Nb^{5+}$ are similar in size to $^{VI}V^{3+}$ and $^{VI}Fe^{3+}$ while $^{VI}Zr^{4+}$ is similar in size to

409    $^{VI}Mg^{2+}$. All except $^{VI}Ce^{4+}$ are smaller than $^{VI}Fe^{2+}$ which is acknowledged to be incorporated in corundum at

410   low levels. Therefore, it seems the exsolution hypothesis cannot be rejected based simply on arguments

411   of ionic radii mismatch. A stronger argument, perhaps, is that cations such as Nb^{5+}, Ta^{5+}, and W^{6+} would

412   be difficult to incorporate in corundum due to both ionic radii mismatch and also their large differences

413   in ionic charge compared to Al^{3+}. In other words, while $^{VI}Nb^{5+}$ and $^{VI}Ta^{5+}$ have the same ionic radii as $^{VI}V^{3+}$,

18

414   they should be much harder to incorporate into the corundum lattice due to the difficulty of substituting

415   a pentavalent cation for Al^{3+}. The presence of such high-field strength elements substituting up to 12

416   atomic % of the Ti in the oriented rutile inclusions studied here, then, seems to be more consistent with

417   a coprecipitation origin for the rutile inclusions rather than exsolution. Such high-field strength elements

418   are, after all, readily incorporated in rutile (Zack et al. 2002). While Cr was not found to be contained

419   within rutile inclusions in this work, oriented oxide inclusions in Cr-rich corundum (ruby) may be an

420   important host for Cr in some cases (e.g. Das and Mohanty 2014).

421   Finally, as suggested above, it is also possible that other nano- or micro-inclusions were

422   contributing to the profile of "unusual" trace elements (i.e. Be, Zr, Nb, Ce, Ta, W) in the LA-ICP-MS data.

423   Given our inability to measure W in our nanoSIMS measurements and in most EPMA analyses, it seems

424   likely that the W measured by LA-ICP-MS is not hosted in some other nano- or micro-inclusion and not

425   the rutile itself. A case can be made that there exists some other inclusions in sample ELA that are

426   enriched in Mg and Be given their close correlation in the LA-ICP-MS measurements. Additionally, from

427   the LA-ICP-MS profiles for sample TUN in **Figure 3**, it is evident that there is a significant increase in Fe

428   concentrations that close follows Ti concentrations. Both Fe and Ti increase significantly crossing over

429   from the inclusion-free rim and into the cloudy, included core. While Raman spectroscopy only

430   determined the presence of rutile inclusions in this sample, it is possible that there also exists some

431   other type of inclusion such as hematite or ilmenite that was overlooked but which could explain the

432   jump in Fe concentrations. Further work should explore the relationship between corundum and other

433   types of oriented oxide inclusions more fully.

434   **Implications**

435   LA-ICP-MS analysis has become the most commonly employed method for obtaining trace

436   element chemistry of gem corundum. The aim of such analyses is generally to find a chemical fingerprint

19

437   identifying the geographic origin of sapphires and rubies or to create genetic classifications in order to

438   develop geological models for the formation of gem corundum. In both regards, understanding the

439   origin of oriented rutile (and other oxide) inclusions is of the utmost importance in the interpretation of

440   trace element data. Given that most oriented oxide inclusions are in the range of 1-2 µm in size while

441   LA-ICP-MS analyses typically measure spots of ~20-60 µm in diameter, measurements of corundum

442   containing a high-density of oriented oxide inclusions will necessarily sample a mechanical mixture of

443   corundum and oxide inclusions. If the inclusions can be assumed to have exsolved from the corundum

444   then the LA-ICP-MS analyses in these included regions do represent the original chemistry of corundum

445   at the time of its formation. However, if the oriented rutile inclusions in these regions were simply

446   coprecipitated along with the corundum, then the LA-ICP-MS analyses do not represent primary

447   corundum but a mixture of primary corundum and primary rutile. Given the evidence presented here for

448   an origin of oriented rutile inclusions by epitaxial coprecipitation, we would argue that LA-ICP-MS

449   analyses of corundum with oriented rutile inclusions should not be assumed *de facto* to represent the

450   original composition of the corundum.

451   All of this is not to say that LA-ICP-MS analyses of cloudy regions in corundum have no use in

452   geographical fingerprinting or in unraveling the genetic history of ruby and sapphire deposits. In fact,

453   the common presence of "unusual" trace elements in such cloudy regions such as Be, Zr, Nb, Ce, Ta, W,

454   and Sn actually has some potential to provide additional trace elements to discriminate between rubies

455   and sapphires from different deposits, assuming there are consistent trace element patterns in the

456   oriented rutile inclusions. In the context of interpretation of geological conditions of formation, it should

457   be understood that when such "unusual" trace elements are found it is likely that they represent the

458   composition of syngenetic rutile and not the corundum itself. However, as long as these trace elements

459   are interpreted in the framework of rutile trace element chemistry, the analysis of such included

460   corundum may still provide some important clues as to the genesis of gem corundum. As a general

20

461   recommendation, we would suggest that, unless otherwise stated, LA-ICP-MS analyses of gem

462   corundum should be performed on regions that have been verified to be inclusion free. This will require

463   careful microscopic examination beforehand, preferably using different illumination techniques

464   (darkfield and brightfield illumination, transmitted light, fiber optic illumination). If regions with a high

465   density of oriented inclusions are observed, it may still be worthwhile to sample such zones, but when

466   the data are reported it should be clearly indicated that such analyses were performed on included

467   areas. Photomicrographic documentation of laser ablation spots may also be helpful in many cases.

468   One such potential application is in the use of the Zr-in-rutile geothermometer for oriented

469   rutile inclusions in corundum containing melt inclusions. Assuming zircon saturation, the

470   geothermometer then only requires the presence of quartz or a measurement of the silica activity of the

471   system. In this case, the silicate melt can be considered to buffer the silica activity of the system

472   allowing the geothermometer to be applied given appropriate thermodynamic corrections. It would

473   then only be required that microanalysis of such oriented rutile inclusions can be performed to

474   accurately measure their Zr contents. Note, however, that this geothermometer could not be used if the

475   rutile inclusions are interpreted to have exsolved from the corundum as it would then be nearly

476   impossible to constrain the silica activity or assume zircon saturation. Another possible application

477   would be in the measurement of Mg contents in oriented rutile inclusions. Meihold (2010) showed that

478   mantle-derived rutile typically contains greater than 200 ppm Mg while rutile with a crustal affinity has

479   Mg less than 200 ppm. If oriented oxide inclusions can be interpreted to be syngenetic rather than

480   exsolved, measurements of their Mg contents could provide an indication of whether the corundum was

481   derived from the Earth's mantle or crust.

482   Furthermore, the interpretation of oriented rutile inclusions in corundum becomes important is

483   in the geological classification schemes devised and employed by many to distinguish between

21

484   metamorphic, magmatic, and metasomatic rubies and sapphires. Some of the discriminant diagrams

485   developed in these efforts, in fact, use Ti as a discriminant element. The results obtained using such

486   classifications, then, may be skewed when analyzing included or silky sapphire. The data presented here

487   suggest that in addition to oriented rutile inclusions, our LA-ICP-MS analyses may also have sampled Mg-

488   rich inclusions. This possibility is also important as Mg is used extensively to classify sapphires and rubies

489   as either metamorphic or magmatic using the measured Ga/Mg ratio. The data for samples AND, ELA,

490   and TUN are plotted on the Ga/Mg vs. Fe discriminant diagram devised by Peucat et al. (2007) in **Figure**

491   **6**. Both AND and ELA show a wide spread in values of Ga/Mg. However, as seen in **Figure 3** all of these

492   samples have relatively constant concentrations of Ga and so variations in Ga/Mg are largely related to

493   varying Mg contents. Indeed, close examination of the data in **Tables S1a-b** along with the

494   photomicrographs in **Figures 2a-d** shows that the high values of Ga/Mg (or low Mg) correspond to the

495   inclusion-free rims while the lower values of Ga/Mg (or high Mg) correlate with the cloudy, included

496   regions. In fact, for sample AND, LA-ICP-MS analyses in the inclusion-free rim would seem to indicate a

497   magmatic origin while analyses in the cloudy, included region would appear to suggest a metamorphic

498   origin. Clearly, the correct interpretation of minute inclusions in gem corundum (i.e. exsolved vs.

499   coprecipitated) is of the utmost importance if LA-ICP-MS data can be used to infer geological conditions

500   of formation. Furthermore, oriented hematite and ilmenite inclusions are also present in some gem

501   corundum. Fe is also used in many discriminant diagrams and, hence, if LA-ICP-MS analyses sample

502   these inclusions it could lead to misclassification using such discriminant diagrams.

503   While included areas may be useful in geographic fingerprinting, in order to unravel geological

504   conditions of corundum formation (i.e. metamorphic vs. magmatic), it is necessary to use trace element

505   data that can be safely assumed to represent only the composition of the original corundum and not

506   rutile which may have coprecipitated with it. In other words, for this sort of work LA-ICP-MS spots

507   should be placed in inclusion-free areas. A full understanding of the controls on trace element chemistry

22

508   of corundum may still not be at hand and the same can be said of rutile. However, altering our

509   interpretation of rutile-included corundum may help us come to a more complete understanding of the

510   trace element systematics in both systems.

511   **Acknowledgments**

519   **References Cited**

520   Ague, J.J., and Eckert, J.O. (2012) Precipitation of rutile and ilmenite needles in garnet: Implications for

521   extreme metamorphic conditions in the Acadian Orogen, U.S.A. American Mineralogist, 97, 840-855.

522   Beran, A., and Rossman, G.R. (2006) OH in naturally occurring corundum. American Mineralogist, 18,

523   441-447.

524   Berg, R.B., and Dahy, J.P. (2002) Montana sapphires and speculation on their origin. Industrial Minerals

525   and Extractive Industry Geology. Geological Society, London, 199-204.

526   Berger, A.L., and Berg, R.B. (2006) The Silver Bow sapphire occurrence, Montana: evidence for a volcanic

527   bedrock source for Montana's alluvial sapphire deposits. Economic Geology, 101, 679-684.

528   Chitty, W. (2009) A study of sapphires and rubies from Tanzania's Tunduru district. B.Sc. Thesis. Kingston

529   University, London.

530   Das, S.K. and Mohanty, J.K. (2014) Characterisation of eluvial corundum (ruby) from Kermunda,

531   Kalahandi District, Odisha, India. Journal of Geology and Geosciences, 3, 180.

532   De Maesschalck, A.A., and Oen, I.S. (1989) Fluid and mineral inclusions in corundum from gem gravels in

533   Sri Lanka. Mineralogical Magazine, 53, 539-545.

534   Emmett, J.L., and Douthit, T.R. (1993) Heat treating the sapphires of Rock Creek, Montana. Gems &

535   Gemology, 29, 250-272.

536   Emmett, J.L., Scarratt, K., McClure, S.F., Moses, T., Douthit, T.R., Hughes, R., Novak, S., Shigley, J.E.,

537   Wang, W., Bordelon, O., and Kane, R.E. (2003) Beryllium diffusion of ruby and sapphires. Gems &

538   Gemology, 39, 84-135.

539   Giuliani, G., Ohnenstetter, D., Fallick, A.E., Groat, L., and Fagan, A.J. (2014) The geology and genesis of

540   gem corundum deposits. In L.A. Groat, Ed., Geology of Gem Deposits, p. 29-112. Mineralogical

541   Association of Canada.

542   Gübelin, E.J., and Koivula, J.I. (2008) Photoatlas of Inclusions in Gemstones, v. 3, Opinio Publishers,

543   Basel, Switzerland.

544   Guo, J., O'Reilly, S.Y., and Griffin, W.L. (1996) Corundum from basaltic terrains: a mineral inclusion

545   approach to the enigma. Contributions to Mineralogy and Petrology, 122, 368-386.

546   Hoe, T.G., Kiong, C.K., and Abd Abiz, bin J.H. (2007) EMPA characterisation of struverite from amang of

547   Peninsular Malaysia. Geological Society of Malaysia, Bulletin, 53, 125-128.

548   Hughes, R.W. (1997) Ruby & Sapphire, 512 p. PWH Publishing, Boulder, Co.

24

549   Hwang, S.L., Yui, T.-F., Chu, H.-T., Shen, P., Schertl, H.P., Zhang, R.Y., and Liou, J.G. (2007) On the origin of

550   oriented rutile needles in garnet from UHP eclogites. Journal of Metamorphic Geology, 25, 349-362.

551   Hwang, S.L., Shen, P., Chu, H.-T., Yui, T.-F., and Iizuka, Y. (2015) Origin of rutile needles in star garnet and

552   implications for interpretation of inclusion textures in ultrahigh-pressure metamorphic rocks. Journal of

553   Metamorphic Geology, 33, 249-272.

554   Izokh, A.E., Smirnov, S.Z., Egorova, V.V., Anh, T.T., Kovyazin, S.V., Phuong, N.T., and Kalinina, V.V. (2010)

555   The conditions of formation of sapphire and zircon in the areas of alkali-basaltoid volcanism in Central

556   Vietnam. Russian Geology and Geophysics, 51, 719-733.

557   Lu, R., and Shen, A.H. (2011) Unusually high beryllium in three blue sapphires. Gems & Gemology, 47,

558   232-233.

559   McGee, B.M. (2005) Characteristics and origin of the Weldborough sapphire, NE Tasmania, 118 p. B.Sc.

560   thesis, University of Tasmania, Hobart.

561   Moon, A.R., and Phillips, M.R. (1984) An electron microscopy study of exsolved phases in natural black

562   Australian sapphire. Micron and Microscopica Acta, 15, 143-146.

563   Peucat, J.J., Ruffault, P., Fritsch, E., Bouhnik-Le Coz, M., Simonet, C., and Lasnier, B. (2007) Ga/Mg ratio

564   as a new geochemical tool to differentiate magmatic from metamorphic blue sapphires. Lithos, 98, 261-

565   274.

566   Phillips, D.S., Heuer, A.H., and Mitchell, T.E. (1980a) Precipitation in star sapphire I. Identification of the

567   precipitate. Philosophical Magazine A, 42, 385-404.

568   Phillips, D.S., Heuer, A.H., and Mitchell, T.E. (1980b) Precipitation in star sapphire II. Elastic

569   accommodation of the precipitate. Philosophical Magazine A, 42, 405-416.

25

570   Phillips, D.S., Heuer, A.H., and Mitchell, T.E. (1980c) Precipitation in star sapphire III. Chemical effects

571   accompanying precipitation. Philosophical Magazine A, 42, 417-432.

572   Pownceby, M.I., Constanti-Carey, K.K., and Fisher-White, M.J. (2003) Subsolidus Phase Relationships in

573   the System Fe_2O_3–Al_2O_3–TiO_2 between 1000° and 1300°C. Journal of the American Ceramic Society, 86,

574   975-980.

575   Rakotondrazafy, A.F.M., Giuliani, G., Ohnenstetter, D., Fallick, A.E., Rakotosamizanany, S.,

576   Andriamamonjy, A., Ralantoarison, T., Razanatseheno, M., Offant, Y., Garnier, V., Maluski, H, Dunaigre,

577   C., Schwarz, D, Ratrimoa, V. (2008) Gem corundum deposits of Madagascar: A review. Ore Geology

578   Reviews, 34, 134-154.

579   Robertson, A.D.C., and Sutherland, F.L. (1992) Possible origins and ages for sapphire and diamond from

580   the central Queensland gem fields. Records of the Australian Museum, Supplement 15, 45A54.

581   Roy, S., and Coble, R.L. (1968) Solubilities of Magnesia, Titania, and Magnesium Titanate in Aluminum

582   Oxide. Journal of the American Ceramic Society, 51, 1-6.

583   Schmetzer, K., Steinbach, M.P., Gilg, A., and Blake, A.R. (2015) Dual-color double stars in ruby, sapphire,

584   and quartz: cause and historical account. Gems & Gemology, 51, 112-143.

585   Shannon, R.D. (1976) Revised effective ionic radii and systematic studies of interatomic distances in

586   halides and chalcogenides. Acta Crystallographica, A32, 751-767.

587   Shen, A.H., and Wirth, R. (2012) Beryllium-bearing nano-inclusions identified in untreated Madagascar

588   sapphire. Gems & Gemology, 48, 150-151.

589   Silva, K.K.M.W., and Siriwardena, C.H.E.R. (1988) Geology and the origin of the corundum-bearing skarn

590   at Bakamuna, Sri Lanka. Mineralium Deposita, 23, 186-190.

26

591   Sutherland, F.L., Graham, I.T., Pogson, R.E., Schwarz, D., Webb, G.B., Coenraads, R.R., Fanning, C.M.,

592   Hollis, J.D., and Allen, T.C. (2002) The Tumbarumba basaltic gem field, New South Wales: In relation to

593   sapphire-ruby deposits of eastern Australia. Records of the Australian Museum, 54, 215-248.

594   Sutherland, F.L., Giuliani, G., Fallick, A.E., Garland, M., and Webb, G. (2009) Sapphire-ruby

595   characteristics, west Pailin, Cambodia: Clues to their origin based on trace element and O isotope

596   analysis. The Australian Gemmologist, 23, 329-368.

597   Upton, B.G.J., Hinton, R.W., Aspen, P., Finch, A., and Valley, J.W. (1999) Megacrysts and associated

598   xenoliths: Evidence for migration of geochemically enriched melts in the upper mantle beneath

599   Scotland. Journal of Petrology, 40, 935-956.

600   Zack, T., Kronz, A., Foley, S.F., and Rivers, T. (2002) Trace element abundances in rutiles from eclogites

601   and associated garnet mica schists. Chemical Geology, 184, 97-122.

602   Ziegler, J.F., Ziegler, M.D., and Biersack, J.P. (2010) SRIM – The stopping and range of ions in matter

603   (2010). Nuclear Instruments and Methods in Physics Research Section B: Beam Interactions with

604   Materials and Atoms, 268, 1818-1823.

605   Zwaan, J.C., Buter, E., Mertz-Kraus, R., and Kane, R.E. (2015) The origin of Montana's alluvial sapphires.

606   Gems & Gemology, 51, 370-391.

607

608   **Figure Captions**

609   **Figure 1:** Photomicrographs of glassy melt inclusions associated with oriented rutile inclusions in

610   sapphires from (a) Rock Creek, Montana, USA - ROC, (b,c) Anakie, Queensland, Australia - ANA, and (d)

611   Missouri River, Montana, USA - MIS.

27

612   **Figure 2:** Photomicrographs of cloudy, rutile-included metamorphic sapphires from (a,b)

613   Andranondambo, Madagascar - AND, (c,d) Elahera, Sri Lanka - ELA, and (e,f) Tunduru, Tanzania - TUN.

614   Positions of LA-ICP-MS analyses are numbered.

615   **Figure 3:** LA-ICP-MS trace element profiles across samples AND, ELA, and TUN in atomic parts per million

616   (ppma). Analysis numbers across the horizontal axis correspond to the numbering scheme employed in

617   photomicrographs of Figure 2a-f.

618   **Figure 4:** Plots of Mg vs. Ti concentrations in atomic parts per million (ppma). The black line is a 1:1 line

619   for equal concentrations of Mg and Ti.

620   **Figure 5:** nanoSIMS raster maps for isotopes of ^{50}Ti, ^{9}Be, ^{56}Fe, and ^{181}Ta for samples (a) AND and (b) TUN.

621   "Cts" represents the number of counts.

622   **Figure 6:** Plot of Fe vs. Ga/Mg for samples AND, ELA, and TUN in parts per million by weight (ppmw)

623   from LA-ICP-MS measurements. Discriminant fields for "metamorphic" and "magmatic" sapphires from

624   Peucat et al. (2007).

625

28

626

627   **Tables**

Table 1A: LA-ICP-MS analyses of sample AND in atomic ppm (ppma)													
Analysis	Be	Mg	Ti	V	Cr	Fe	Ga	Zr	Nb	Ce	Hf	Ta	W
1	bql*	14.1	14.0	2.25	1.3	946	19.71	bql	bql	0.0017	bql	bql	bql
2	bql	11.0	12.0	2.65	1.2	933	21.38	bql	bql	bql	bql	bql	bql
3	bql	9.7	8.9	2.94	1.3	925	21.79	bql	bql	bql	bql	bql	bql
4	bql	45.0	85.1	2.61	1.2	1000	22.17	0.143	bql	0.0015	0.0078	bql	bql
5	bql	73.6	95.0	3.46	1.3	1050	22.87	0.376	1.122	0.0020	0.0115	0.1781	12.3099
6	bql	78.1	178.0	3.41	1.2	1120	24.07	0.416	0.548	0.0025	0.0126	0.0879	5.4563
7	1.09	76.8	138.0	3.41	1.3	1100	23.02	0.813	1.108	0.0070	0.0274	0.1615	11.3118
8	bql	73.5	121.0	3.21	1.1	1070	23.49	0.291	0.802	0.0023	0.0086	0.1341	9.7038
9	bql	71.2	113.0	3.15	1.1	1040	22.58	0.241	0.714	0.0031	0.0055	0.1330	9.0051
10	bql	32.3	123.0	2.49	1.5	908	20.88	0.134	0.009	bql	0.0025	0.0020	0.0821
11	bql	12.7	10.9	1.87	2.4	778	30.61	bql	bql	bql	bql	bql	0.0043
12	bql	64.7	70.9	2.45	1.2	958	22.43	0.295	0.236	bql	0.0105	0.0248	1.8853
13	bql	76.4	165.0	3.36	1.5	1040	23.28	0.152	0.486	0.0019	0.0041	0.0879	5.2456
14	0.63	74.2	147.0	3.37	1.4	1040	22.35	0.366	0.739	0.0025	0.0137	0.1161	7.3638
15	0.81	74.0	124.0	3.30	1.5	1010	23.17	0.969	1.504	0.0068	0.0274	0.2220	14.4170
16	bql	73.8	169.0	3.24	1.4	1000	22.41	0.130	0.180	bql	0.0039	0.0428	2.4953
17	bql	56.6	91.0	2.77	1.8	917	20.88	0.072	0.189	bql	0.0014	0.0462	2.3844
standard deviation	0.27	0.2	0.5	0.04	0.3	4	0.01	0.004	0.003	0.0004	0.0002	0.0003	0.0003
detection limit	0.18	0.1	0.3	0.03	0.2	3	0.01	0.003	0.002	0.0003	0.0001	0.0002	0.0002
*bql = below quantitation limit = 3.33×detection limit													

628

629

29

630

631

Table 1B: LA-ICP-MS analyses of sample ELA in atomic ppm (ppma)													
Analysis	Be	Mg	Ti	V	Cr	Fe	Ga	Zr	Nb	Ce	Hf	Ta	W
1	bql*	42.8	30.8	4.98	0.9	213	16.38	bql	bql	0.0019	bql	0.0010	bql
2	bql	38.8	26.3	4.33	1.3	204	16.18	bql	bql	0.0022	bql	bql	bql
3	bql	65.2	42.1	3.65	1.1	200	15.68	bql	bql	0.0028	0.0007	0.0047	bql
4	bql	99.3	67.6	4.14	1.1	220	15.82	bql	bql	0.0036	0.0006	0.0104	bql
5	bql	132.6	103.9	4.75	1.1	233	16.56	0.010	bql	0.0063	0.0047	0.0293	bql
6	1.49	132.6	115.9	4.52	1.4	226	16.38	0.034	0.023	0.0076	0.0112	0.5218	0.0111
7	bql	99.3	82.9	4.25	1.1	217	15.71	bql	bql	0.0032	0.0024	0.0338	0.0011
8	bql	134.2	119.7	4.64	1.3	221	15.91	0.010	bql	0.0070	0.0030	0.1691	0.0026
9	1.20	161.1	284.1	5.54	1.3	239	16.88	0.093	0.22	0.2064	0.0240	5.7815	0.1264
10	9.47	361.6	125.7	4.54	1.2	277	17.14	0.011	0.009	0.0113	0.0021	0.0845	0.0011
11	1.11	140.1	128.2	4.54	1.3	260	17.08	bql	0.009	0.0038	bql	0.0316	0.0017
12	bql	133.4	136.3	4.40	1.4	241	17.32	bql	bql	0.0047	bql	0.0023	bql
13	bql	132.6	203.6	4.52	1.5	225	16.94	0.018	0.011	0.0083	0.0023	0.4959	0.0024
14	1.15	101.5	80.4	4.24	1.1	211	14.86	bql	bql	0.0087	0.0045	0.0902	0.0035
15	bql	152.7	247.5	5.42	1.1	245	16.58	0.088	0.184	0.1673	0.0171	4.9363	0.1187
16	24.98	578.1	741.2	7.77	1.3	324	19.48	0.079	0.167	0.3880	0.0160	2.4681	0.1155
17	2.41	251.7	655.0	7.79	1.3	267	19.54	0.044	0.095	0.1310	0.0027	1.0864	0.0499
18	bql	145.1	137.6	4.63	1.3	251	17.67	bql	0.004	0.0035	bql	0.0372	0.0014
19	bql	143.4	134.6	4.94	1.3	262	17.99	bql	bql	0.0036	0.0030	0.0234	bql
20	bql	162.8	164.0	5.52	1.4	278	18.55	bql	0.007	0.0306	bql	0.1037	0.0111
21	bql	157.7	503.7	6.36	1.0	262	19.60	0.101	0.815	5.4854	0.0171	8.1708	0.4605
22	5.09	521.9	494.2	6.33	1.0	305	18.49	0.101	0.331	0.3884	0.0160	5.2754	0.1464
23	3.60	182.1	330.2	6.04	1.5	256	19.22	0.067	0.156	0.3114	0.0126	3.6289	0.0955
24	bql	135.1	125.7	4.68	1.4	238	17.32	0.018	0.018	0.0175	0.0030	0.2874	0.0027
standard deviation	0.27	0.2	0.5	0.039	0.3	4	0.01	0.004	0.003	0.0004	0.0002	0.0003	0.0003
detection limit	0.18	0.1	0.3	0.026	0.2	3	0.01	0.003	0.002	0.0003	0.0001	0.0002	0.0002
*bql = below quantitation limit = 3.33×detection limit													

632

633

30

634

635

Table 1C: LA-ICP-MS analyses of sample TUN in atomic ppm (ppma)													
Analysis	Be	Mg	Ti	V	Cr	Fe	Ga	Zr	Nb	Ce	Hf	Ta	W
1	bql*	125.9	109.1	3.96	1.0	94.3	8.980	bql	bql	bql	bql	bql	bql
2	1.67	130.0	196.4	4.45	1.5	154	9.653	0.101	0.014	bql	0.0126	0.3460	0.0095
3	1.29	110.7	317.8	4.24	1.4	148	9.809	0.065	0.077	0.0087	0.0066	0.7100	0.0998
4	bql	133.4	111.6	3.82	1.3	159	10.033	bql	bql	bql	bql	0.0037	0.0059
5	bql	161.9	498.4	6.39	1.2	174	11.261	1.114	5.729	0.9472	0.1119	40.1212	27.1405
6	bql	167.0	400.0	6.45	1.6	188	12.344	0.740	3.710	0.3929	0.0685	34.0354	16.3023
7	bql	176.2	461.1	6.47	1.5	183	12.461	0.946	4.478	0.5340	0.0971	34.0354	17.5222
8	bql	158.6	165.7	5.46	1.5	171	11.729	0.085	0.342	0.0274	0.0046	2.5696	0.3392
9	bql	141.0	127.8	4.08	1.4	151	10.384	0.014	bql	bql	bql	0.0164	0.0071
10	bql	141.0	127.8	4.24	1.4	147	10.413	0.091	bql	bql	0.0018	0.0042	bql
11	bql	131.7	366.8	4.61	1.6	154	10.618	0.592	0.204	0.0067	0.0274	1.5645	0.1841
12	bql	102.7	86.7	3.62	1.5	152	9.828	bql	bql	bql	bql	bql	bql
13	bql	81.4	70.1	3.68	1.7	139	9.867	bql	bql	bql	bql	bql	bql
14	bql	120.8	114.6	3.56	bql	144	9.114	0.017	bql	bql	0.0024	0.1555	bql
15	1.58	113.3	97.8	3.72	1.7	148	9.305	bql	bql	0.0010	bql	0.0237	bql
16	1.09	104.0	110.3	3.69	Bql	144	9.365	bql	bql	bql	0.0022	0.0451	bql
17	1.86	108.2	341.2	3.65	Bql	150	9.414	0.037	0.021	0.0023	0.0040	0.2186	bql
18	bql	137.6	115.4	3.87	bql	146	10.208	0.009	bql	bql	bql	0.0039	bql
19	bql	145.1	414.4	4.23	bql	155	10.442	0.523	0.099	0.0063	0.0217	0.8746	0.1594
20	0.85	148.5	183.6	4.13	1.9	158	10.355	0.062	0.034	0.0015	bql	0.2592	0.0494
21	bql	134.2	262.0	4.08	bql	157	10.345	0.101	0.057	bql	0.0160	0.6807	0.0721
22	1.22	123.3	109.4	3.76	bql	151	9.806	bql	bql	bql	bql	0.0123	bql
standard deviation	0.27	0.2	0.5	0.04	0.3	4	0.009	0.004	0.003	0.0004	0.0002	0.0003	0.0003
detection limit	0.18	0.1	0.3	0.03	0.2	2	0.006	0.002	0.002	0.0003	0.0001	0.0002	0.0002
*bql = below quantitation limit = 3.33×detection limit													

636

637

31

638

Table 2: EPMA analyses of oriented rutile inclusions in samples TUN and ELA

wt%	TUN1	TUN2	TUN3	ELA1	ELA2	ELA3
TiO_2	72.91	75.24	72.68	96.88	96.65	94.35
FeO_{tot}	2.40	2.32	2.21	0.42	0.79	0.63
MgO	0.60	0.68	0.51	0.00	0.05	0.02
Ta_2O_5	22.40	20.35	22.39	1.57	0.95	3.76
V_2O_3	0.39	0.11	0.23	0.12	0.00	0.28
WO_3	0.00	0.00	0.00	0.00	0.00	0.35
Nb_2O_5	1.31	1.26	1.53	0.00	0.64	0.00
ZrO_2	0.00	0.00	0.45	0.33	0.44	0.26
Ce_2O_3	0.00	0.00	0.32	0.43	0.41	0.29

atoms per formula unit (per 2 O atoms)

	TUN1	TUN2	TUN3	ELA1	ELA2	ELA3
Ti	0.8450	0.8603	0.8419	0.9839	0.9730	0.9709
Fe^{2+}	0.0313	0.0299	0.0289	0.0048	0.0090	0.0073
Mg	0.0137	0.0154	0.0116	0.0001	0.0011	0.0005
Ta	0.0940	0.0842	0.0939	0.0058	0.0035	0.0140
V	0.0048	0.0013	0.0028	0.0013	0.0000	0.0031
W	0.0000	0.0000	0.0000	0.0000	0.0000	0.0012
Nb	0.0091	0.0086	0.0107	0.0000	0.0039	0.0000
Zr	0.0000	0.0000	0.0034	0.0022	0.0029	0.0017
Ce^{4+}	0.0000	0.0000	0.0017	0.0020	0.0019	0.0014

Note: Data are corrected by removing Al_2O_3 and renormalizing to 100 wt% as described in the text

639

640

32

641

Table 3: Ionic radii of potential substitional cations in corundum[1]		
	r(Å)	% difference from Al^{3+}
Be^{2+}	0.45	15.9
Mg^{2+}	0.72	34.6
Al^{3+}	0.535	0.0
Ti^{4+}	0.605	13.1
V^{3+}	0.64	19.6
Cr^{3+}	0.615	15.0
Fe^{2+}	0.78	45.8
Fe^{3+}	0.645	20.6
Ga^{3+}	0.62	15.9
Zr^{4+}	0.72	34.6
Nb^{5+}	0.64	19.6
Ta^{5+}	0.64	19.6
W^{6+}	0.6	12.1
Ce^{4+}	0.87	62.6

[1]Shannon (1976) with high spin $Fe^{2+, 3+}$.
Ionic radii reported for octahedral coordination by six O^{2-} anions.
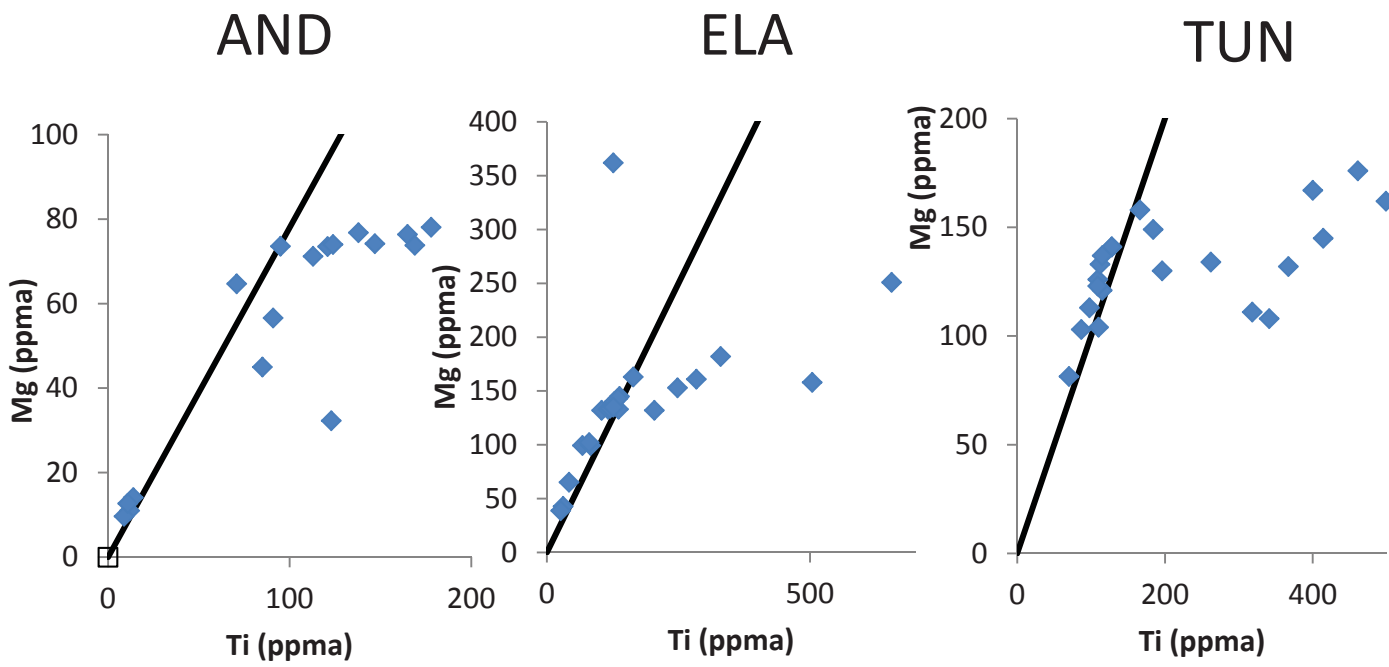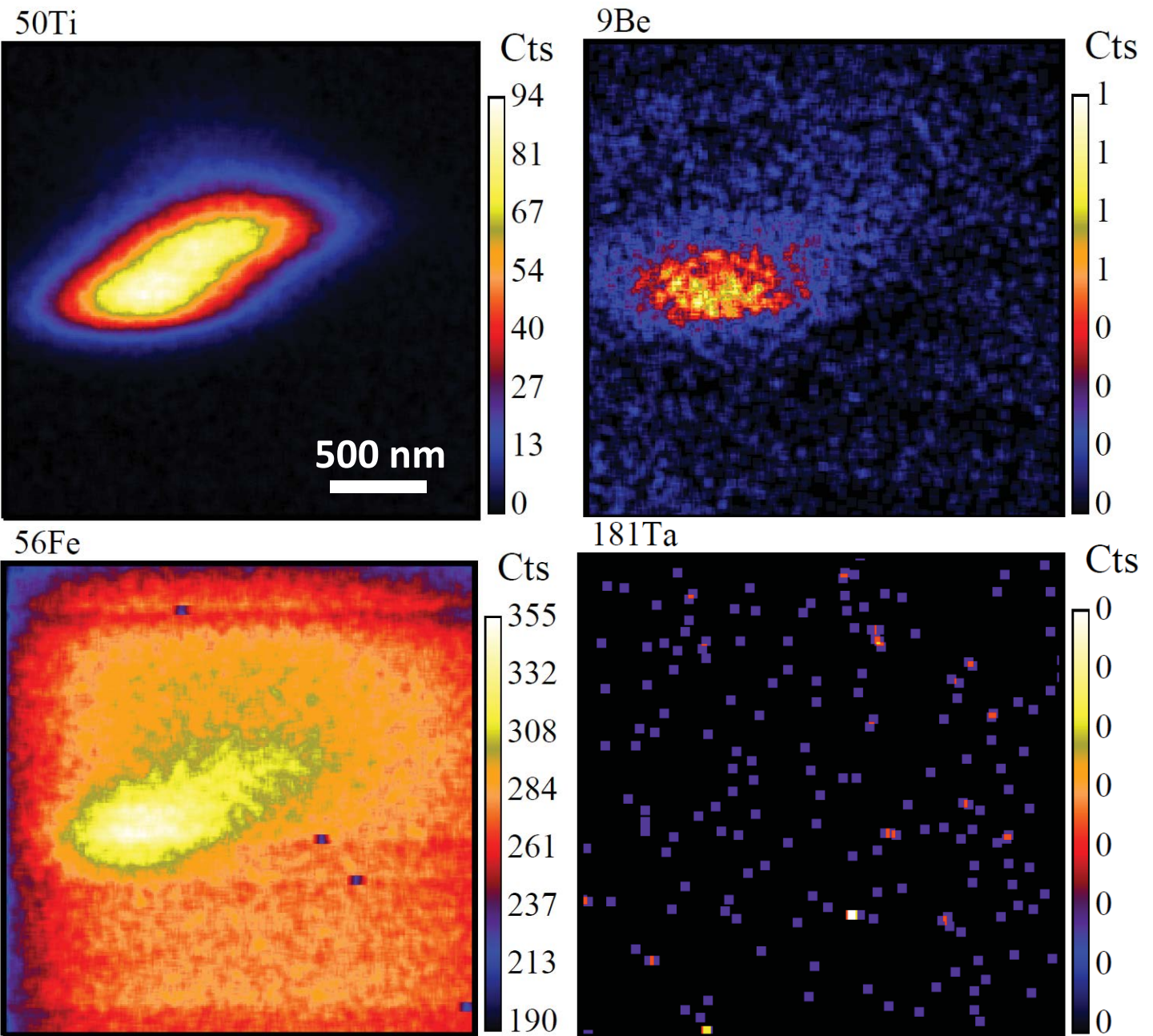
642

643

33
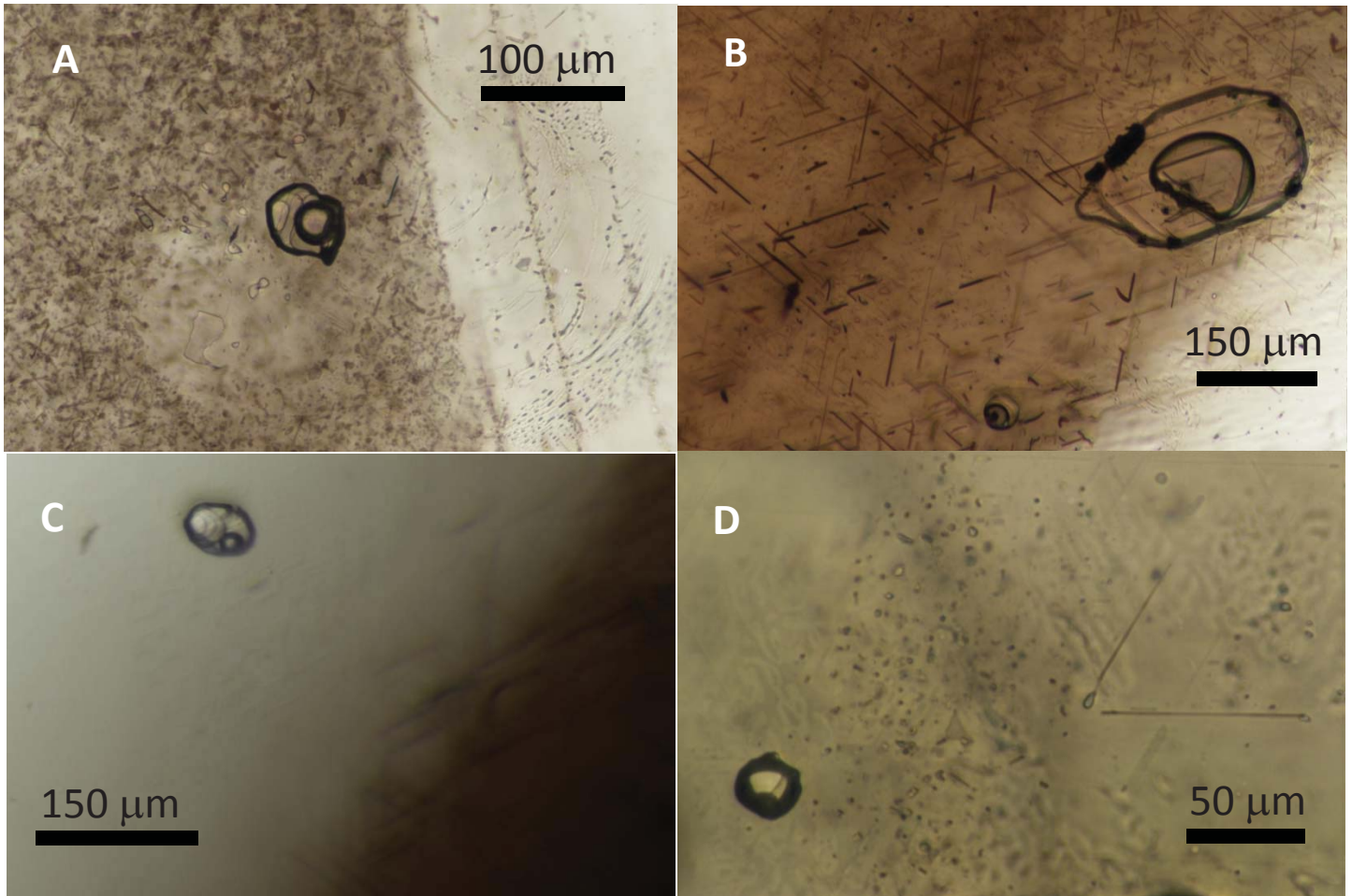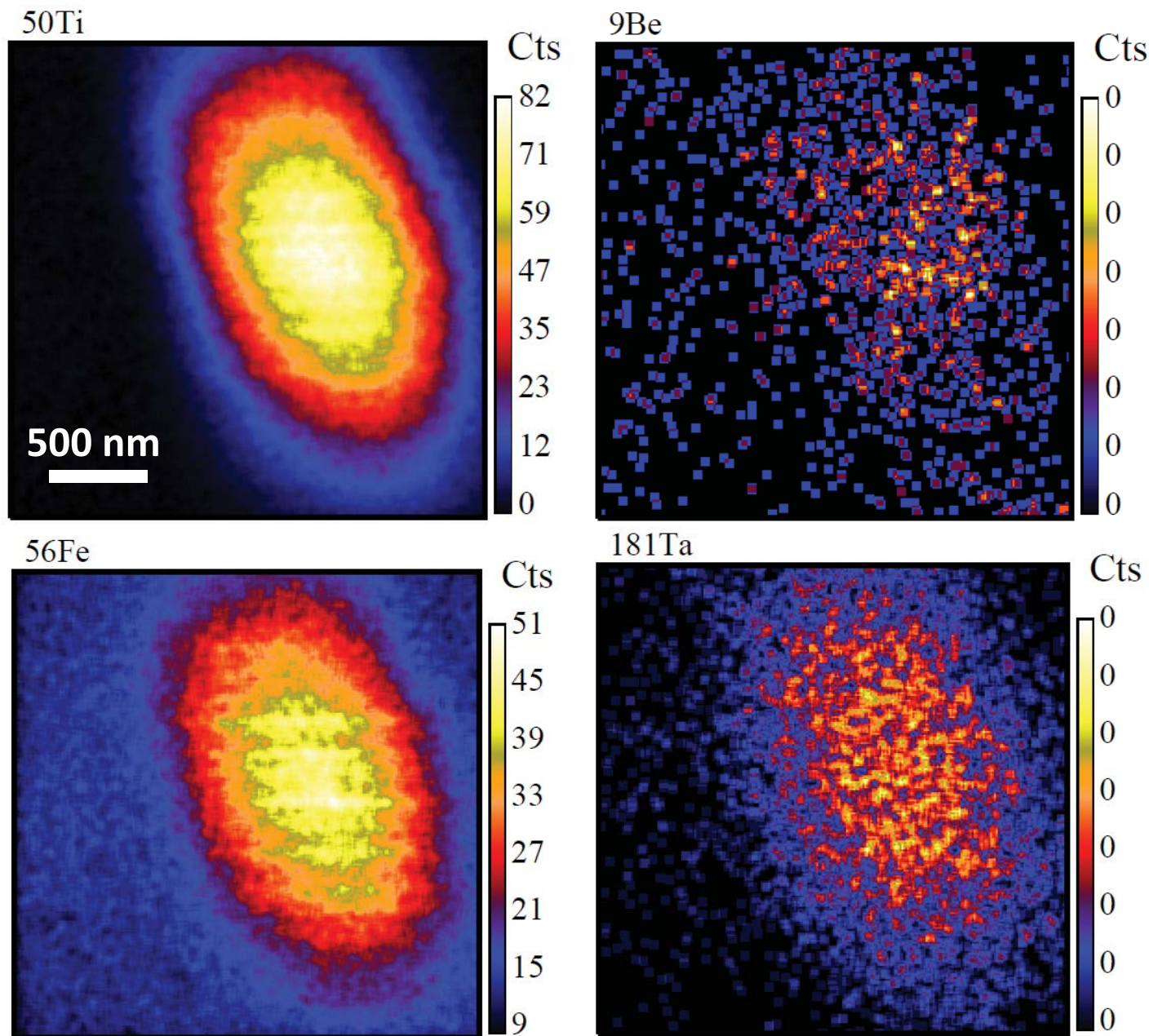
Figure 1

Figure 1

Figure 2
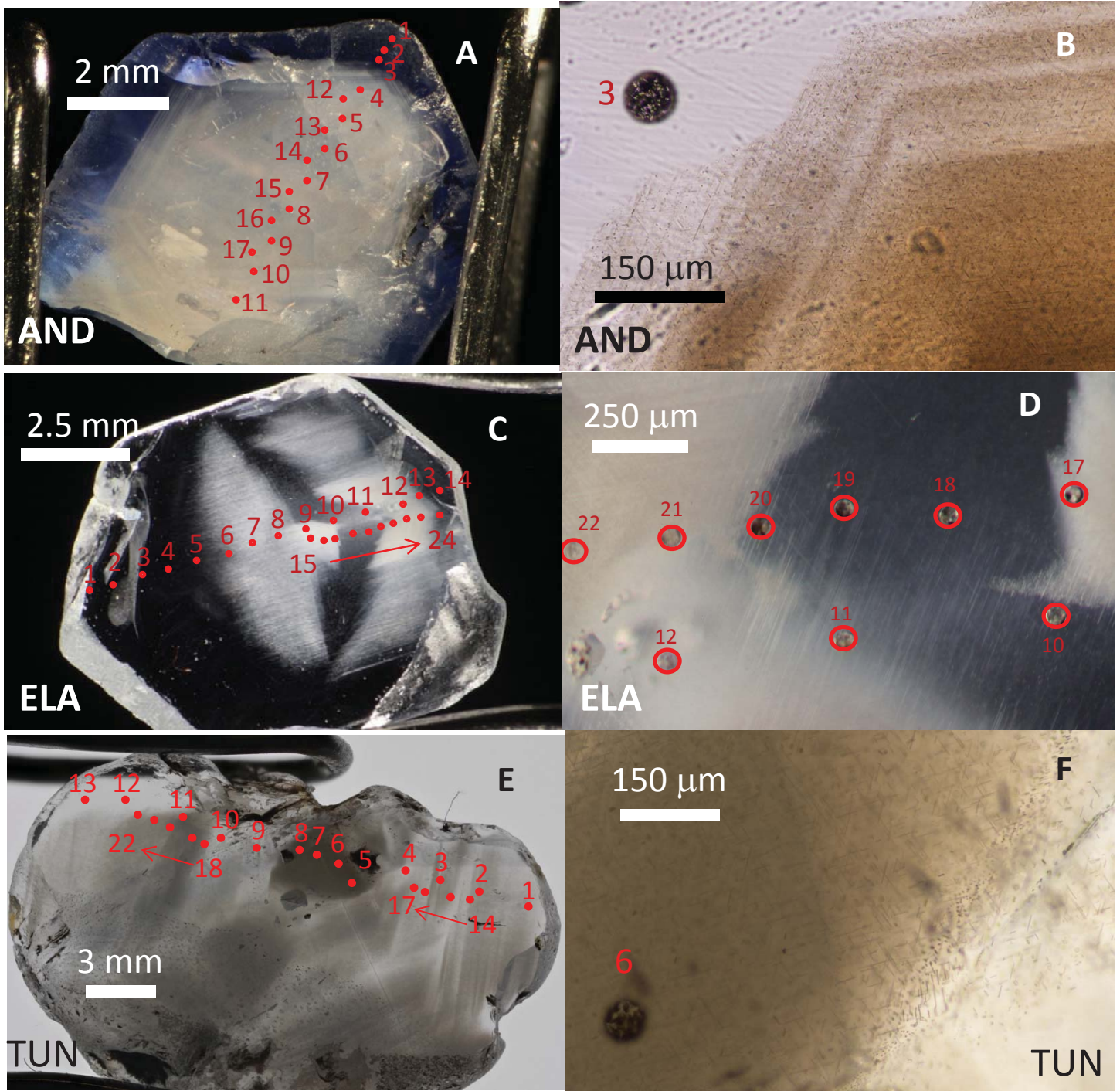
Figure 3
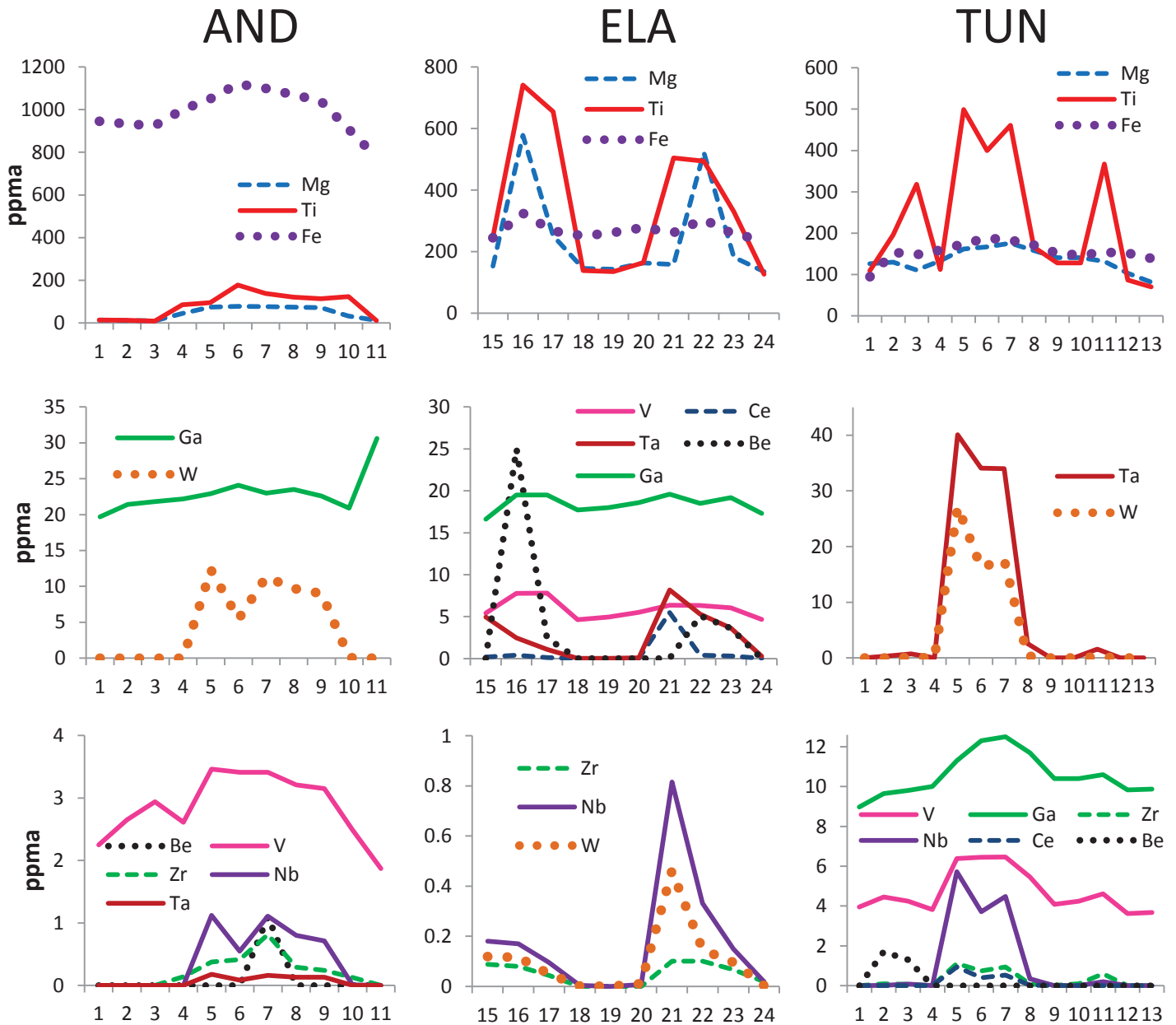
Figure 4

Figure 5a

AND

Figure 5b

TUN

Figure 6